AIAA AVIATION Forum
12-16 June 2023, San Diego, CA and Online
AIAA AVIATION 2023 Forum

10.2514/6.2023-3690

Conservative and Robust Compact Finite Difference Approach for Simulations of Dense Gas Flows

Hang Song[1], Aditya S. Ghate[2], Steven Dai[1], Anjini Chandra[1], and Sanjiva K. Lele[1,2]
[1]*Department of Mechanical Engineering, Stanford University, Stanford, CA 94305, USA*
[2]*Department of Aeronautics & Astronautics, Stanford University, Stanford, CA 94305, USA*

Supercritical fluids have a number of thermodynamic and chemical properties which make them attractive for use in environmentally friendly technologies. However, though the thermodynamic properties of supercritical fluids have been studied comprehensively, the dynamics of supercritical and transcritical fluid flows are less well explored and understood. Studying the behavior of such fluid flows through high-quality computational investigations could provide crucial insights useful for designing and controlling flow systems operating in supercritical and transcritical regimes. An accurate and robust computational framework is a prerequisite to conducting high-quality computational investigations. This work extends a high-fidelity computational framework for ideal gas flows by including complex thermodynamic models and realistic transport models near the critical point of the fluid where abrupt changes in density and transport properties occur with small temperature or pressure fluctuations. The spatial discretization is based on compact finite difference methods that achieve high-order grid convergence and the high spectral resolution needed to resolve small scale flow structures. The computational approach achieves robustness by reducing the aliasing error and improving the spectral resolution of the viscous fluxes at high wavenumbers. No non-conservative correction or filtering is needed to maintain robustness for shock-free flows if physical or physics-based model dissipation is included. The framework is also compatible with applications of shock capturing schemes and approximated Riemann solvers and supports simulations on curvilinear meshes. Two problems involving compressible free-shear flows (temporal mixing layer) and wall-bounded flows (zero-pressure gradient flat plate boundary layer with a cold isothermal wall) are studied for dense gases to demonstrate the robustness and versatility of the proposed numerical formulation.

I. Introduction

Supercritical fluids have recently drawn increasing attention in many industrial applications due to their superior physical and chemical properties [1, 2]. As an example, supercritical CO_2 power cycles offer key advantages in energy conversion due to their compactness, high thermal efficiency, and longer life cycles due to corrosion resistance. They can operate with a variety of heat sources, including sustainable sources, such as geothermal power, concentrated solar power and high temperature fuel cells, nuclear reactors, and traditional fossil fuels [3]. A pure fluid reaches the supercritical state when both its pressure and temperature are above the critical point. Transitioning between subcritical and supercritical states, the fluid undergoes a pseudo phase change where the thermodynamic and transport properties, e.g., density, viscosity, thermal conductivity, vary significantly within a narrow range of temperature and pressure. Unlike the ideal gas, a fluid near the critical point exhibits complex thermodynamic behavior. The pressure-specific volume-temperature (p-v-T) relation is highly nonlinear. Additionally, the specific internal energy is dependent on both temperature and density (or specific volume) and accounts for the effects of intermolecular interactions. Due to the complexities introduced by the behaviors of thermodynamic and transport properties, numerical solutions of flows in this regime require special consideration. In many cases, when a flow of a transcritical or supercritical fluid is turbulent, the significant variations in thermodynamic and transport properties of the fluid are highly coupled with the fluid motions which further increases the complexity of the turbulence dynamics.

Numerical computations have been utilized to investigate the flows of dense gases. However, for the fully compressible system, abrupt changes in thermodynamic properties, especially density, associated with a small range of temperature and pressure variation may cause severe and spurious oscillation [4, 5]. There are two common methods used to address this problem in the simulations. The first approach is to rely on the extra numerical dissipation, especially around the pseudo-phase change regions [4, 6], and the second approach is to introduce a total energy correction [7] or replace

the energy equation by the pressure evolution equation [5]. However, both of these modifications achieve numerical robustness at the cost of sacrificing simulation accuracy to some degree. Excessive numerical dissipation tends to damp the physically growing high wavenumber features. If numerical dissipation is applied as a dominant mechanism in the computational approach, the local simulation results should be considered as physically under-resolved solutions. Careful assessment of fine-scale features is required to establish physical realism of the simulated results.

In simulations of transcritical flows, the abrupt density changes are determined by the equation of state (EOS) and are caused by physical density and pressure fluctuations in the flow. During the pseudo-phase change from the subcritical state to the supercritical state, or vice versa, the density change associated with pressure and temperature is still smooth. Therefore, in a shock-free flow, there is no discontinuity in the flow during pseudo-phase change. The simulation quality thus primarily depends on the tolerance of the simulation framework to the dispersion and aliasing error without excessive numerical dissipation. Pressure-based solvers can effectively reduce the spurious oscillations in the simulation results. However, this robustness is at a cost of breaking the discrete conservation. For a fully compressible system, this treatment is not favorable for simulations of flows with shock waves, especially with their complexity in non-ideal thermodynamic fluids.

This work proposes a unified simulation framework for simulations of transcritical fluid flows. The conservative formulation of the computational systems for ideal gas flows is preserved. Additionally, the spatial discretization is based on compact finite difference schemes and compact interpolations to achieve both high-order grid convergence and highly improved spectral resolution [8]. The EOS and transport properties are calculated using physics-based models that resolve the abrupt changes in properties during pseudo phase changes. In this manuscript, the mathematical formulation of the problem and the associated physical closure models are described in Sec. II, the numerical solution methods are summarized in Sec. III, and some demonstrative computational results for simulations of a compressible planar shear layer and turbulent boundary layer are presented and discussed in Sec. IV.

II. Mathematical formulation and physical models

In this section, the mathematical model used for numerical simulations is described. The computations can be conducted in either dimensional or dimensionless form. A consistent non-dimensionalization is provided here for the governing equations and closure physical models for the thermodynamic and transport properties.

A. Governing equations

The simulation solves the compressible Navier-Stokes equations including conservation of mass, momentum, and total energy:

$$\frac{\partial \rho}{\partial t} + \frac{\partial \rho u_j}{\partial x_j} = 0 \tag{1}$$

$$\frac{\partial \rho u_i}{\partial t} + \frac{\partial}{\partial x_j}\left(\rho u_i u_j + p\delta_{ij}\right) = \frac{\partial \sigma_{ij}}{\partial x_j} \tag{2}$$

$$\frac{\partial \rho e_{\text{tot}}}{\partial t} + \frac{\partial}{\partial x_j}\left[\left(\rho e_{\text{tot}} + p\right) u_j\right] = \frac{\partial}{\partial x_j}\left(u_i \sigma_{ij} - q_j\right) \tag{3}$$

Here, index notation is applied: ρ is the density, u_i is the velocity vector, p is the pressure, δ_{ij} is the identity tensor, σ_{ij} is the viscous stress tensor, and e_{tot} is the specific total energy which includes the specific internal energy, e, and the specific kinetic energy. e_{tot} is given as follows:

$$e_{\text{tot}} = e + u_j u_j / 2$$

q_j is the heat flux due to the thermal conduction defined as

$$q_j = -\lambda \frac{\partial T}{\partial x_j}$$

where λ is the thermal conductivity, and T is the temperature field. The viscous stress is calculated as

$$\sigma_{ij} = 2\mu S_{ij} + \left(\beta - \frac{2}{3}\mu\right) S_{kk}\delta_{ij} \tag{4}$$

where μ and β are the dynamic shear and bulk viscosities respectively, and $S_{ij} = \frac{1}{2}\left(u_{i,j} + u_{j,i}\right)$ is the rate of strain tensor. The computational system is closed by the EOS and calculation of the transport properties. For a dense gas, the EOS includes the p-v-T relation, i.e., $p = p(\rho, T)$, and the formulation of the internal energy is determined by both density and temperature, or $e = e(\rho, T)$. The transport properties are calculated using the temperature and pressure. The detailed formulations of the EOS and transport models are discussed in the following sub-sections.

B. Thermodynamic models

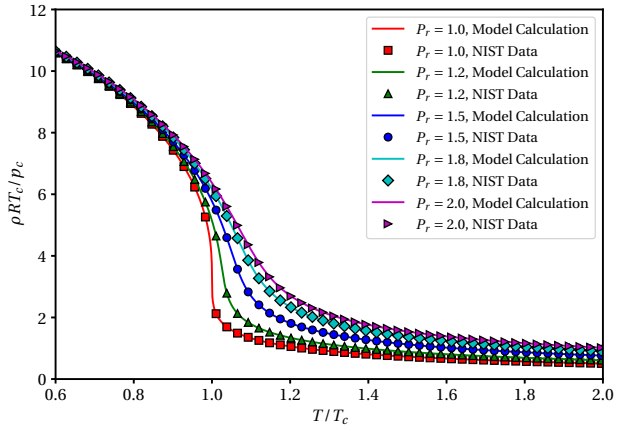

Fig. 1 p-v-T relation calculated from the Peng-Robinson EOS.

For a pure gas near critical conditions, the Peng-Robinson EOS [9] is used for the p-v-T relation. The mathematical expression is provided as follows:

$$p = \frac{RT}{v - b} - \frac{a\alpha(T_r)}{v^2 + 2vb - b^2} \tag{5}$$

where p is the pressure, T is the temperature, R is the specific gas constant, and a and b are model constants defined as

$$a = 0.45723553\frac{R^2T_c^2}{p_c} \qquad \text{and} \qquad b = 0.07779607\frac{RT_c}{p_c} \tag{6, 7}$$

where T_c and p_c are the critical temperature and pressure respectively. T_r in Eq. (5) is the reduced temperature, which is dimensionless, defined as $T_r = T/T_c$. The expression of $\alpha(T_r)$ in Eq. (5) is given as

$$\alpha(T_r) = \left[1 + \kappa\left(1 - \sqrt{T_r}\right)\right]^2 \tag{8}$$

where κ is a quadratic fitting of the acentric factor ω and is given as

$$\kappa = 0.37464 + 1.54226\omega - 0.26992\omega^2 \tag{9}$$

For CO_2, $\omega \approx 0.239$. Eq. (5) implies a non-dimensionalization using p_c, T_c and R, where p_c and T_c provide a pressure and temperature scale respectively. The density scale is defined as $\rho_0 = p_c/(RT_c)$. Furthermore, drawing a parallel to kinematic motion, a velocity scale is derived as $U_0 = \sqrt{RT_c}$. As a side note, ρ_0 and U_0 are results from dimensional analysis that may not be equal to the density or speed of sound at critical conditions. The dimensionless form of Eq. (5) can be written as

$$p_r = \frac{T_r}{v^* - b^*} - \frac{a^*\alpha(T_r)}{v^{*2} + 2v^*b^* - b^{*2}} \tag{10}$$

where $p_r = p/p_c$ is known as the reduced pressure. The superscript "$*$" denotes the non-dimensionalized quantity, and the parameters a^*, b^*, and v^* are given as:

$$a^* = 0.45723553 \qquad b^* = 0.07779607 \qquad v^* = \rho_0 v$$

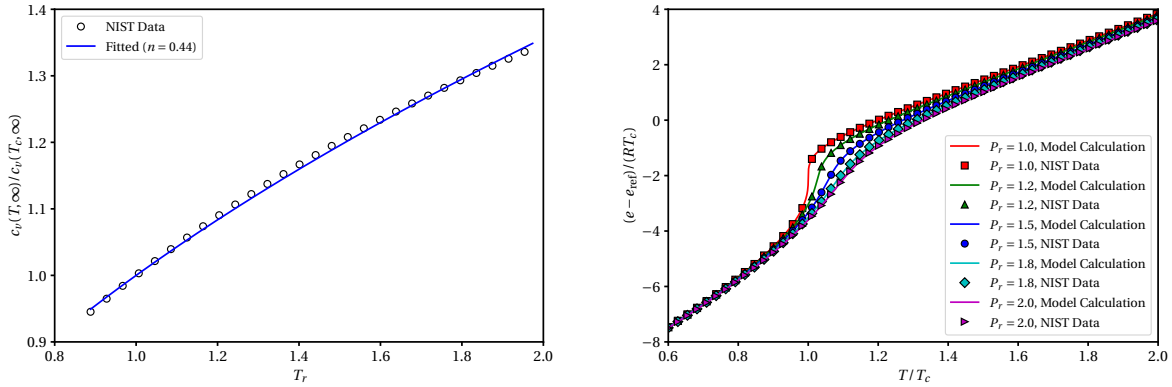

(a) (b)

Fig. 2 Evaluation of the internal energy calculation. (a) Evaluation of specific heat at a constant volume in the ideal gas limit where n is the exponent of the power law fitting defined in Eq. (12) and T_{ref} is chosen to be T_c. The reference solution is obtained from the NIST database [10]. (b) Evaluation of internal energy e in isobaric conditions with P chosen to be P_c and comparison of e against reference values obtained from NIST database [10].

The p-v-T behavior is plotted in Fig. 1. The model parameters are set for CO_2. For reference, the results obtained from the Peng-Robinson EOS are compared with data from the National Institute of Standards and Technology (NIST) Web Book [10]. As shown in Fig. 1, the pseudo phase change behavior is well-captured by the model p-v-T relation near the critical temperature at supercritical pressures.

The internal energy can be calculated using the following equation:

$$e = e_{\text{ref}} + \int_{T_{\text{ref}}}^{T} c_v(T, v_{\text{ref}})dT + \int_{v_{\text{ref}}}^{v} \left[T\left(\frac{\partial p}{\partial T}\right)_v - p \right] dv \tag{11}$$

where c_v is the specific heat at constant volume, and the subscript "ref" indicates a reference state. Eq. (11) indicates a two-step integration along an isochoric path followed by an isothermal path. On the right-hand side of Eq. (11), the second integral can be evaluated by the p-v-T relation from Eq. (5). The first integral, however, requires an additional model for the temperature dependent c_v at a reference specific volume. Taking $v_{\text{ref}} \to \infty$, the reference state is in the ideal gas regime. For certain gases, $c_v(T, \infty)$ can be evaluated based on the following power law for simplicity:

$$c_v(T, \infty) = c_v(T_{\text{ref}}, \infty)\left(\frac{T}{T_{\text{ref}}}\right)^n \tag{12}$$

Using CO_2 as an example, the accuracy of the fitted power law for temperature-dependent c_v in the ideal gas limit is shown in Fig. 2a, and the results are compared to data from the NIST database [10]. The integrated results of the internal energy using Eq. (11) are shown in Fig. 2b, and the results are compared with data from the NIST database as well.

In a compressible flow, the speed of sound, c, is associated with the isentropic pressure change with respect to the density as follows:

$$c^2 = \left(\frac{\partial p}{\partial \rho}\right)_s \tag{13}$$

During simulation, to determine the Courant–Friedrichs–Lewy (CFL)-based adaptive time step [11] as well as the characteristic decomposition and approximate Riemann solver for shock capturing, the speed of sound must be evaluated consistently with the thermodynamic models. Based on the thermodynamic relations, the speed of sound can be calculated as

$$c = v\sqrt{\frac{T}{c_v}\left(\frac{\partial p}{\partial T}\right)_v^2 - \left(\frac{\partial p}{\partial v}\right)_T} \tag{14}$$

where c_v is calculated from the expression for the specific internal energy and the right-hand side of Eq. (14) is determined based on the p-v-T relation. Alternatively, if the expression for pressure, or $p = p(\rho, e)$, is known, the

speed of sound can be calculated equivalently as

$$c = \sqrt{\left(\frac{\partial p}{\partial \rho}\right)_e + \frac{p}{\rho^2}\left(\frac{\partial p}{\partial e}\right)_\rho} \tag{15}$$

C. Transport models

The calculations of a fluid's viscosity and thermal conductivity in the transcritical and supercritical regimes are based on the approach proposed in Chung et al. [12]. The model accounts for the effects of both temperature and pressure. The original version of the model, particularly for the calculation of thermal conductivity, is formulated in a dimensional form for engineering applications. Its utilization requires that quantities be provided in particular physical units. In this work, all the dimensional parameters in the model formulation have been consistently scaled so that the model can be directly used for both dimensional and dimensionless computations.

According to the model from Chung et al., the dynamic shear viscosity of a pure gas is evaluated as

$$\frac{\mu}{\mu_c} = \frac{\mu^*}{\mu_c^*} \tag{16}$$

Here, μ_c is the dynamic shear viscosity at the critical condition defined as $\mu_c = \mu(T_c, p_c)$. μ^* is a dimensionless function of temperature and density, and μ_c^* is μ^* evaluated at the critical condition, or $\mu_c^* = \mu^*(T_c, \rho_c)$. The calculation of μ^* requires a p-v-T relation, and to maintain consistency, the Peng-Robinson model as described in Sec. II.B is used. The expression for μ^* calculated using the Peng-Robinson model is given as

$$\mu^* = \frac{\sqrt{T^*}}{\Omega_v(T^*)} F_c \left(\frac{1}{G_2(\rho^*)} + E_6\rho^*\right) + \eta^{**}(T^*, \rho^*) \tag{17}$$

where the dimensionless temperature T^* is calculated as $T^* = 1.2593T_r$, and the dimensionless density is evaluated as $\rho^* = \rho v_c/6$ with v_c representing the specific volume at the critical condition. The parameters involved in Eq. (17) are determined based on the properties of the gas molecules and detailed in Ref [12] and Ref [13]. In this work, the dynamic bulk viscosity is not included.

Based on the model from Chung et al., the thermal conductivity, λ, can be calculated as

$$\frac{\lambda}{R\mu_c} = 3.75256\mu_r^{\ominus}\Psi(T_r, p_r)\left(\frac{1}{G_2} + E_6\rho^*\right) + q^*E_7G_2\rho^{*2}\sqrt{T_r} \tag{18}$$

where $\mu_r^{\ominus} = \mu^{\ominus}/\mu_c$ is the relative low-pressure dynamic shear viscosity, and the superscript "$\ominus$" denotes that the quantity is evaluated at the same temperature but in the low-pressure regime. The detailed calculations of the model parameters are provided in Ref [12] and Ref [13]. The left-hand side of Eq. (18) implies that the thermal conductivity is consistently scaled by $R\mu_c$, and all calculations involved on the right-hand side of Eq. (18) can be conducted using the non-dimensionalized quantitites.

III. Numerical Scheme (Summary)

All numerical schemes used for collocated-to-edge interpolation and derivative operations are sixth-order compact schemes [14, 15]. The high-order formulation will provide rapid grid convergence. Moreover, compared to explicit schemes, the compact scheme has significantly improved spectral resolution especially in the high wavenumber regime. However, for high-order and high-resolution schemes, numerical stability becomes a major concern [15].

The spatial discretization used in this work is based on the framework proposed by Song et al. [8]. During the solution process, all conservative variables are evolved at the collocated grid points while the fluxes are assembled at the edge-staggered points in each direction respectively. A minimum set of primitive variables, u_i, T, and p, are interpolated from the collocated grid points calculated from the conservative variables to assemble the inviscid fluxes. For the viscous fluxes, the gradient components which are aligned with the flux direction are calculated using staggered first derivative schemes, and the components that are not aligned with fluxes directions are first calculated using the collocated differential schemes and then interpolated from the collocated grid points to the corresponding edge-staggered points. Eventually, the divergence operators are evaluated using staggered first derivative schemes in each direction, and

the results are taken back from the edge-staggered grid points to the collocated grid points. The discretization has been proven to work on both uniform Cartesian meshes and curvilinear wavy meshes.

The discretization method significantly contributes to reducing the aliasing error in the nonlinear inviscid fluxes and resolving the viscous dissipation in the high wavenumber regime including a non-trivial response of the Nyquist viscous dissipation. A more quantitative analysis and mathematical proofs are provided in Song et al. [8]. In simulations of flows in the transcritical regime, the pseudo phase change of the fluid amplifies the aliasing error originating from the calculation of temperature and pressure. The small spurious oscillations in the pressure and temperature fields may lead to noticeable fluctuations in the mass flux that cause the numerical error to grow. The proposed simulation framework addresses this issue by providing sufficient dealiasing during the assembly of the nonlinear fluxes. Additionally, the high spectral resolution of the compact schemes used in the simulation framework significantly reduces the dispersion error. Furthermore, the non-trivial response of the viscous dissipation at the Nyquist wavenumber damps the grid-to-grid oscillations which makes the computational system more stable. The numerical filtering operations, claimed to be necessary in many compact scheme based framework, can be avoided.

In addition, for flows at transcritial conditions, the pseudo phase change behavior is physically regularized by the EOS model on the macro scale. Therefore, the rapid density change associated with a relatively small temperature fluctuation during the pseudo phase change should be a numerically well-resolved feature. This requires numerical framework to have high spectral resolution and low numerical dispersion to resolve the solution profile with a large local gradient and curvature.

For highly compressible flows, shocks may develop. In the proposed simulation framework, all the fluxes are assembled at the edge-staggered grid points. The solution approach is naturally compatible with the non-linear shock-capturing scheme combined with an approximate Riemann solver. As a result, a hybrid central-Riemann flux is assembled. In simulations of compressible turbulent flows, the numerical dissipation is desired to highly locate at the shock structures to artificially capture the under-resolved features. In the shock-free region, the turbulent flow behavior should only rely on the physical or physics-based model dissipation.

In this work, the flux blending is controlled by a physics-based shock sensor that is modified from the Ducros sensor. The mathematical formulation of the modified Ducros sensor, ϕ, is given in the following equation:

$$\phi = \frac{-|\theta|\,\theta + \varepsilon^2}{\theta^2 + \boldsymbol{\omega}\cdot\boldsymbol{\omega} + \varepsilon^2} \tag{19}$$

Here, $\theta = \nabla\cdot\boldsymbol{u}$ is the velocity dilatation, $\boldsymbol{\omega} = \nabla\times\boldsymbol{u}$ is the vorticity vector, and $\varepsilon = 1\times10^{-16}$ is used for round-off regularization. According to the equation, in a non-uniform flow, $\phi < 0$ indicates local expansion, and $\phi > 0$ indicates local compression. During simulation, a threshold sensor value, ϕ_{TH}, is specified. If $\phi > \phi_{\mathrm{TH}}$, Riemann fluxes will be used. Otherwise, only central fluxes will be used.

IV. Demonstrative computations

Results from idealized unit test problems are not shown in this paper. Instead, results from high-resolution, three-dimensional turbulent flow simulations in two illustrative problems are shown. These problems are intended as a numerical demonstration of the success of the proposed method in simulating realistic turbulent flows.

A. Planar shear layer

The basic configuration of the compressible shear layer simulation is shown in Fig. 3. The computational domain size is $L_x\times L_y\times L_z = 12\pi\times20\times6\pi$, and the mesh size is $N_x\times N_y\times N_z = 1024\times512\times512$. The computational domain is periodic in the $x-$ and $z-$ directions, and the computational mesh is uniform along these two dimensions. The computational mesh is stretched in y-direction to use majority of the grid points to resolve the growth of the shear layer. Near the upper and lower domain boundaries in the y-direction, numerical sponge layers are applied to enforce the far-field flow condition on each side. The base flow velocity is parallel to the x-direction with variation in y-direction. The initial base flow velocity profile, U_0, is regularized with a finite shear layer thickness using the following hyperbolic tangent profile:

$$U_0(y) = \frac{U_{+\infty}+U_{-\infty}}{2} + \frac{U_{+\infty}-U_{-\infty}}{2}\tanh\left(C_\delta\frac{y}{\delta_0}\right) \tag{20}$$

where $U_{+\infty}$ and $U_{-\infty}$ are constants representing the far-field velocities on the upper and lower sides of the domain respectively. The dimensionless constant C_δ is a scaling factor that defines the characteristic velocity based on the shear

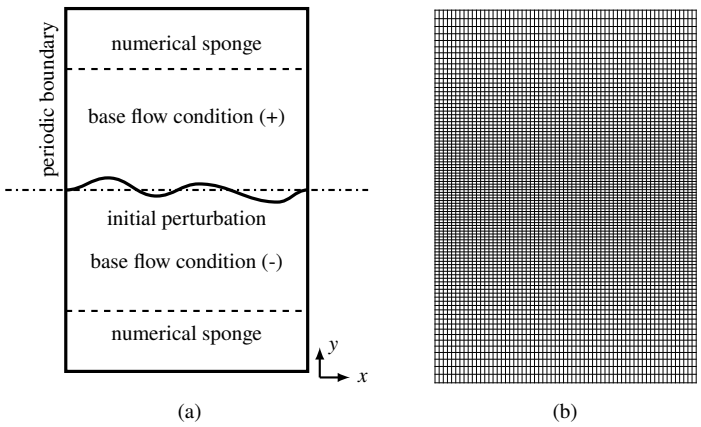

Fig. 3 Simulation configuration of compressible planar shear layer: (a) configuration of computational domain; (b) computational mesh. The computational domain is periodic in z-direction, and the computational mesh is uniform in x and z.

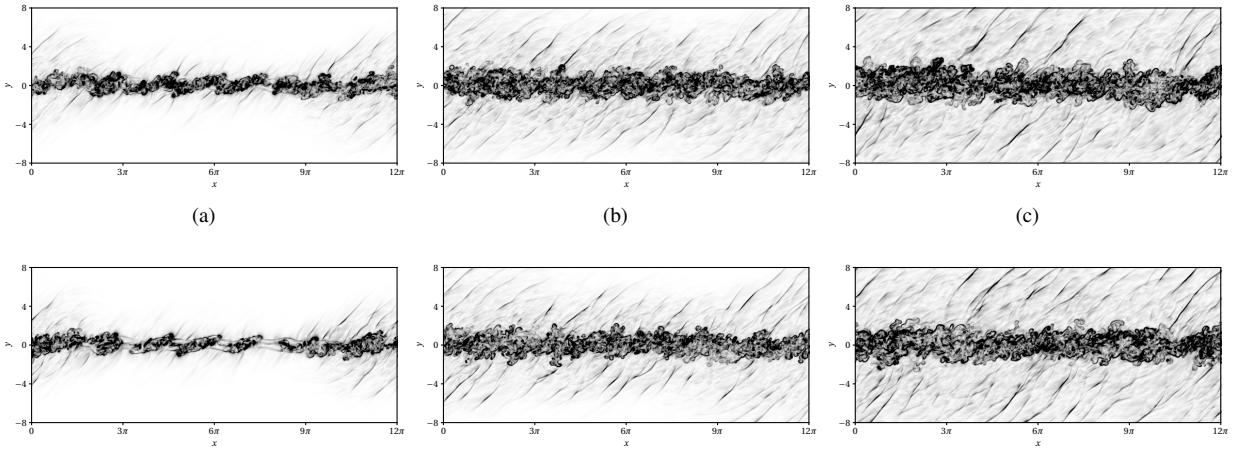

Fig. 4 Numerical Schlieren imaging of the planar shear layers: (a), (b), and (c) are the visualizations of the supercritial CO_2 flow at the normalized time, τ, 500, 600, and 700 respectively; (d), (e), and (f) are the visualizations of the calorically perfect gas at the same corresponding normalized times.

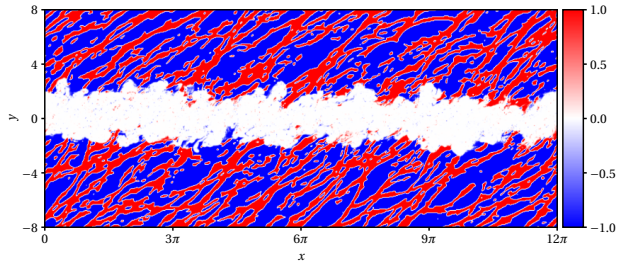

Fig. 5 Visualization of the modified Ducros sensor in the dense gas shear layer at $\tau = 700$. The modified Ducros sensor is defined in Eq. (19). The flow is at same state as shown in Fig. 4c.

layer thickness δ_0. In this simulation, $C_\delta = 2\tanh^{-1}(0.99)$, and δ_0 represents the shear layer thickness such that the edge velocity matches 99% of the far-field velocity. The momentum thickness, δ^{**}, for an instantaneous velocity profile is defined as

$$\delta^{**} = \frac{1}{\rho_{-\infty}U_{-\infty}} \int_{-\infty}^{0} \overline{\rho}\widetilde{u}\,(U_{-\infty} - \widetilde{u})\,dy + \frac{1}{\rho_{+\infty}U_{+\infty}} \int_{0}^{+\infty} \overline{\rho}\widetilde{u}\,(U_{+\infty} - \widetilde{u})\,dy \tag{21}$$

where $\rho_{-\infty}$ and $\rho_{+\infty}$ are the far-field densities in the lower and upper sides of the domain respectively. The operator $\overline{(\cdot)}$ denotes the Reynolds averaging within the x-z plane at each y location, and the operator $\widetilde{(\cdot)}$ denotes the Favre averaging, such that $\widetilde{(\cdot)} = \overline{\rho(\cdot)}/\overline{\rho}$. The convective Mach number M_c is defined as

$$M_c = \frac{|U_{+\infty} - U_{-\infty}|}{c_{+\infty} + c_{-\infty}} \tag{22}$$

where $c_{+\infty}$ and $c_{-\infty}$ are the far-field speeds of sound on the upper and lower sides of the domain respectively. The Reynolds numbers are defined as

$$\mathrm{Re}_\delta = \rho_0 \frac{|U_{+\infty} - U_{-\infty}|\,\delta}{\mu_0} \qquad \text{and} \qquad \mathrm{Re}_{\delta^{**}} = \rho_0 \frac{|U_{+\infty} - U_{-\infty}|\,\delta^{**}}{\mu_0} \tag{23, 24}$$

where ρ_0 and μ_0 are the characteristic density and dynamic shear viscosity respectively. In this demonstrative simulation, the initial temperature and pressure are uniform. The initial reduced pressure is $p_{r0} = 1.8$, and the initial reduced temperature is $T_{r0} = 1.4$. Accordingly, ρ_0 and μ_0 in (23) and Eq. (24) are the initial density and viscosity respectively. Based on the symmetry of the problem, the far-field velocities are set as $U_{+\infty} = -U_{-\infty} = U_\infty$ for $U_\infty > 0$. As an initial condition, a wide-band velocity perturbation is prescribed within the shear layer. The simulation is configured with $M_c = 1$. The initial Reynolds numbers are $\mathrm{Re}_\delta \approx 2232$ and $\mathrm{Re}_{\delta^{**}} \approx 243$ respectively. The time advancement is conducted using the third-order strong stability preserving Runge-Kutta method (SSP-RK3) [16] with CFL = 0.6.

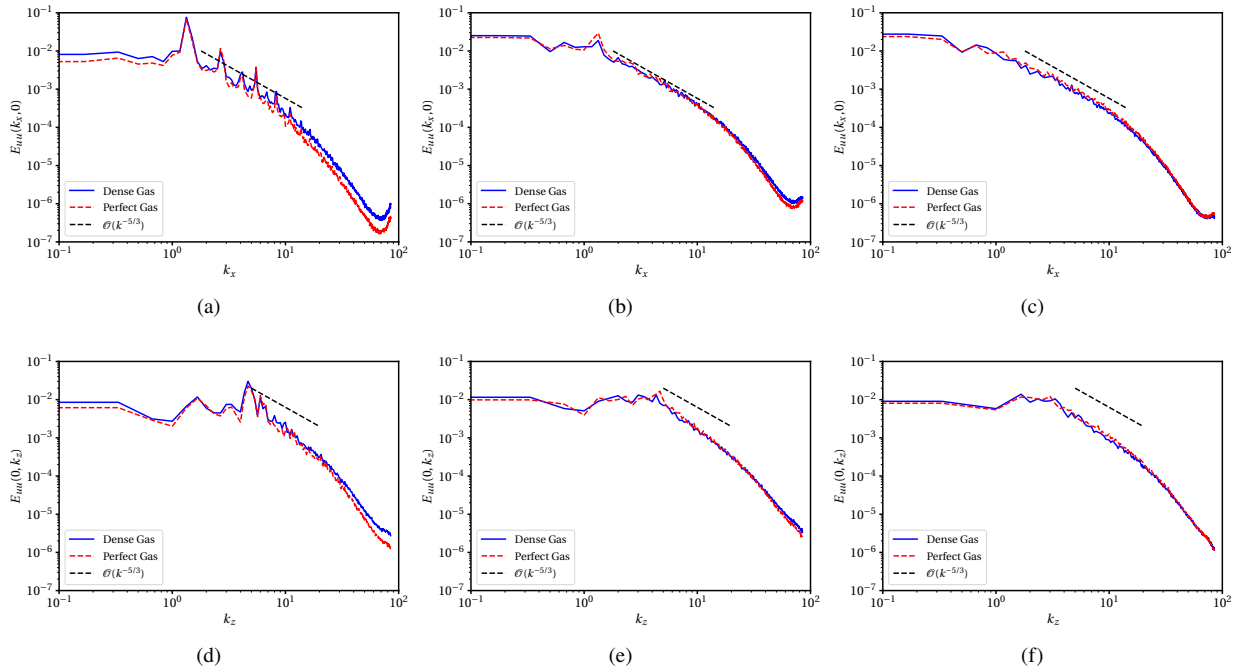

Fig. 6 One-dimensional streamwise velocity energy spectra at the center plane $y = 0$: (a) and (d): $\tau = 500$; (b) and (e): $\tau = 600$; (c) and (f): $\tau = 700$.

As a comparison, a calorically perfect gas flow is also simulated with identical configurations. In the simulation of the calorically perfect gas flow, the dynamic shear viscosity is calculated as $\mu = \mu_0(T_r/T_{r0})^{0.76}$. The thermal conductivity is calculated as $\lambda = c_p\mu/\mathrm{Pr}$, where c_p is the specific heat at constant pressure evaluated as $c_p = \gamma R/(\gamma - 1)$, and the Prandtl number, Pr is assumed to be constant Pr = 0.7. The ratio of the specific heats, γ, is a constant, and $\gamma = 1.4$ here.

A convective nondimensional time, τ, is introduced as

$$\tau = tU_\infty/\delta_0^{**} \tag{25}$$

Visualizations of the simulation results are shown in Fig. 4 using numerical Schlieren imaging, $|\nabla\rho|$, at τ = 500, 600, and 700 respectively. For comparison, the visualizations of the dense gas flow and perfect gas flow are shown at the same normalized convective time. The numerical Schlieren imaging visualizations show that in both simulations, the turbulent shear layer structures generate significant Mach waves and shock waves. In these simulations, the hybrid central-Riemann flux is used as described in Sec. III. The threshold sensor value is set to be $\phi_{\text{TH}} = 0.4$. The Riemann flux is assembled in the Rusanov form [17] with the fifth-order weighted essentially non-oscillatory interpolation scheme (WENO5-JS) [18] for finite difference methods. An instantaneous visualization of the modified Ducros sensor for the dense gas flow at τ = 700 is shown in Fig. 5. The visualization corresponds to the flow structure shown in Fig. 4c. By comparison, it can be seen that the shock capturing scheme is highly localized to the shock structures, and no artificial dissipation is imposed in the simulation of turbulent flow structures within the shear layer.

The one-dimensional streamwise velocity energy spectra along the streamwise (x) and spanwise (z) directions at different times are shown in Fig. 6. As the turbulent shear layer growth, approximately one decade of turbulent cascade has formed in both the dense gas and perfect gas flows, and there is no significant difference shown in the energy spectra between the two types of flows. At τ = 700, the two-point correlation of the stream-wise velocity at the center plane (y = 0) is shown in Fig. 7. The results indicate that the turbulent structure has sufficient decorrelation in both stream-wise and span-wise directions, and the confinement from the domain periodicity has no noticeable effects on the growth of the turbulent shear layer in both cases.

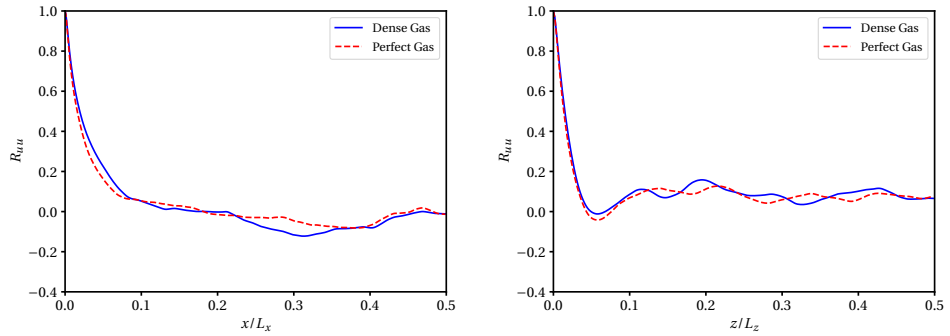

(a) (b)

Fig. 7 Two-point correlation of the stream-wise velocity at the center plane (y = 0): (a) the two-point correlation in x-direction and (b) the two-point correlation in z-direction.

Lastly, the time histories of several flow profiles are provided in Fig. 8 for reference. The fluctuating component corresponding to the Reynolds decomposition is defined as $(\cdot)' = (\cdot) - \overline{(\cdot)}$, and the fluctuating component corresponding to the Favre decomposition is defined as $(\cdot)'' = (\cdot) - \widetilde{(\cdot)}$. The operator "$\langle(\cdot)\rangle$" denotes the domain average defined as

$$\langle(\cdot)\rangle = \frac{1}{\delta^{**}}\int_{-\infty}^{+\infty}\overline{(\cdot)}dy$$

The results show that the turbulent shear layers for the dense gas and perfect gas have similar growth rates measured from momentum thickness and turbulent velocity fluctuations. More noticeable differences are present in the profiles of fluctuating thermodynamic quantities. The dense gas shear layer has a larger fluctuation in density and pressure during the entire history of shear layer growth. However, as the shear layer becomes fully turbulent, the perfect gas flow shows higher temperature fluctuation and the final temperature fluctuations. This phenomenon implies that under the flow conditions, the density fluctuation is primarily due to the turbulent dilatational motion. Comparing the EOS of the dense gas and perfect gas near the critical temperature, the dense gas temperature is significantly less sensitive to the density change. For similar turbulence intensity (Fig. 6), the temperature fluctuation of the dense gas is less affected by the turbulent dilatational motion.

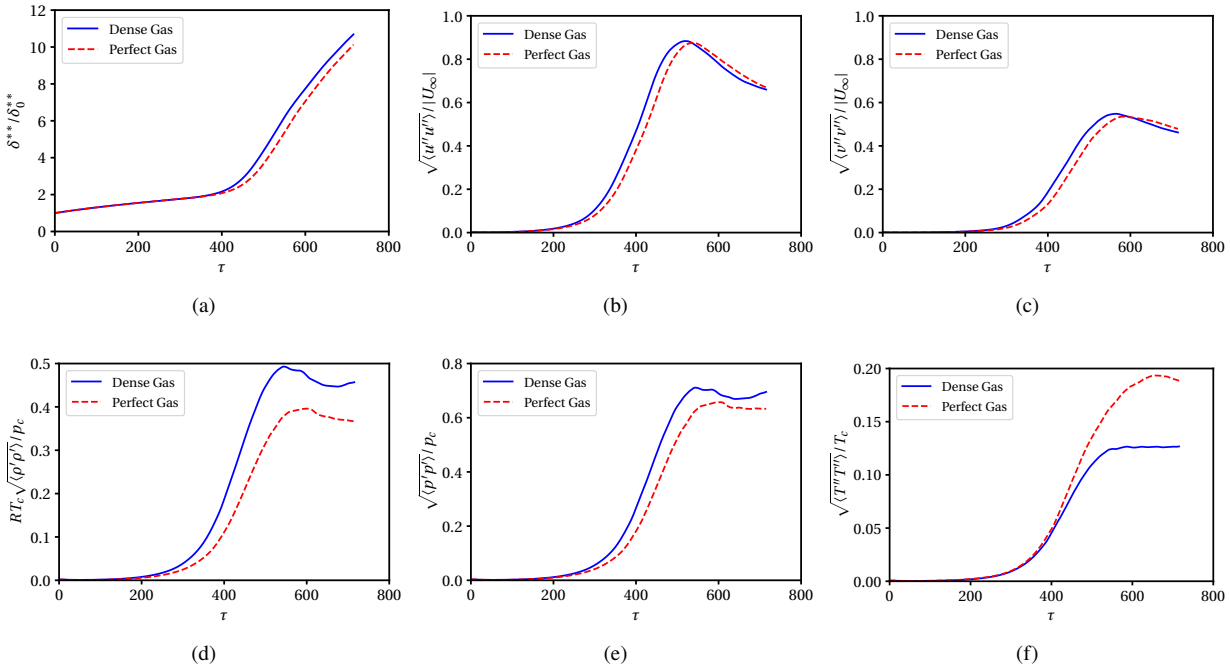

Fig. 8 Time histories of flow properties in growing planar shear layer: (a) momentum thickness; (b) streamwise velocity fluctuation; (c) transverse velocity fluctuation; (d) density fluctuation; (e) pressure fluctuation; and (f) temperature fluctuation.

B. Turbulent boundary layer

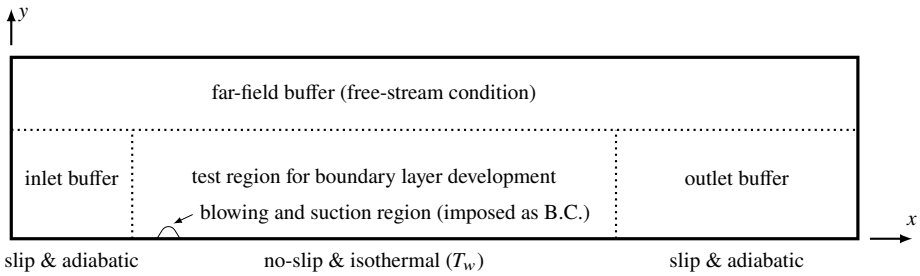

Fig. 9 Simulation configuration of turbulent boundary layer flow.

The basic simulation configuration is shown in Fig. 9. The span-wise direction is homogeneous and periodic (not shown in the schematics). The computational domain in the x-y plane is divided into four sub-regions: the top far-field buffer, inlet buffer, outlet buffer, and the test region where the boundary layer develops. The numerical sponge method is applied to the top far-field region to preserve the free-stream flow conditions. The inlet buffer also contains a numerical sponge to enforce a prescribed inlet flow profile given as a function of y coordinate. The prescribed velocity and temperature profiles are numerically regularized close to the bottom boundary to mimic an infinitesimally thin but numerically resolved boundary layer. The thickness of the numerically regularized inlet boundary layer is denoted as δ_{in}. Beyond the thickness, $y > \delta_{\text{in}}$, the flow is forced to reach the free-stream condition in the inlet buffer region. The density profile in the inlet buffer is calculated using the Peng-Robinson p-v-T relation to preserve the uniform free-stream pressure. The flow in the outlet buffer is damped using the Riemann-flux with the WENO5-JS interpolation scheme, and the homogeneous Neumann boundary condition is applied to the whole flow field at the streamwise boundary. The bottom boundary in the test region is configured as a no-slip adiabatic wall, and the wall temperature is denoted as T_w. The bottom boundary in the inlet and outlet buffer regions are both slip and adiabatic.

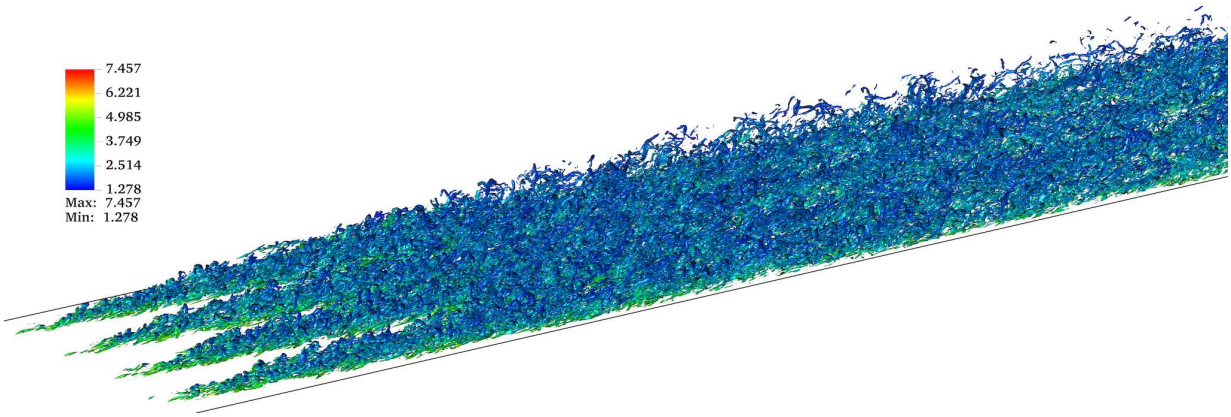

Fig. 10 Visualization of the Q-criterion isosurface of the turbulent boundary layer colored by the non-dimensional density, $\rho RT_c/p_c$.

In order to trigger a transition to turbulence, a narrow region of blowing and suction is introduced in the boundary condition. Within the blowing and suction region, the wall-normal velocity is prescribed as

$$v_b(x,z,t) = W(x;x_{f0},x_{f1}) \sum_{m=-N_f}^{N_f} A_m \sin(\omega_m t - k_m z - \varphi_m) \tag{26}$$

where $W(x;x_{f0},x_{f1})$ is the Hanning windowing function corresponding to the forcing region $x \in (x_{f0},x_{f1})$

$$W(x;x_{f0},x_{f1}) = \frac{1}{2} - \frac{1}{2}\cos\left(2\pi\frac{x-x_{f0}}{x_{f1}-x_{f0}}\right) \tag{27}$$

The rest of terms on the right-hand side of Eq. (26) are a linear combination of $2N_f + 1$ selected temporal-spatial modes, where for each model m, A_m is the mode amplitude, ω_m is the mode frequency, k_z is the wavenumber in the z-direction, and $\varphi_m \sim \mathcal{N}(0,\pi)$ is a Gaussian random number serving as the initial phase shift. In this simulation, $N_f = 4$, $\omega_m = -\omega_{-m}$, $k_m = k_{-m}$. Consequently, v_b contains four pairs of symmetric oblique modes and a stationary mode.

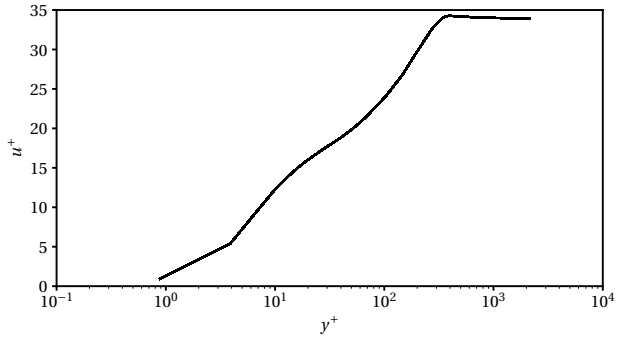

Fig. 11 Scaled stream-wise velocity profile in the wall-normal direction.

The test region size is $200\delta_{\text{in}} \times 40\delta_{\text{in}} \times 10\pi\delta_{\text{in}}$. The total computational mesh size is $2048 \times 384 \times 512$. The computational mesh in the test region is uniform in the x-direction and slightly stretched in the y-direction. The computational mesh in the buffer regions is highly coarsened away from the test region with a large mesh stretch rate in both the x- and y- directions. The computational mesh in z-direction is uniform in the entire computational domain. The free-stream Mach number is $M_\infty = 0.3$, and the freestream reduced temperature and pressure are $T_\infty/T_c = 1.5$ and $p_\infty/p_c = 2$ respectively. The reduced temperature at the isothermal wall is $T_w/T_c = 0.95$. The temperature specification

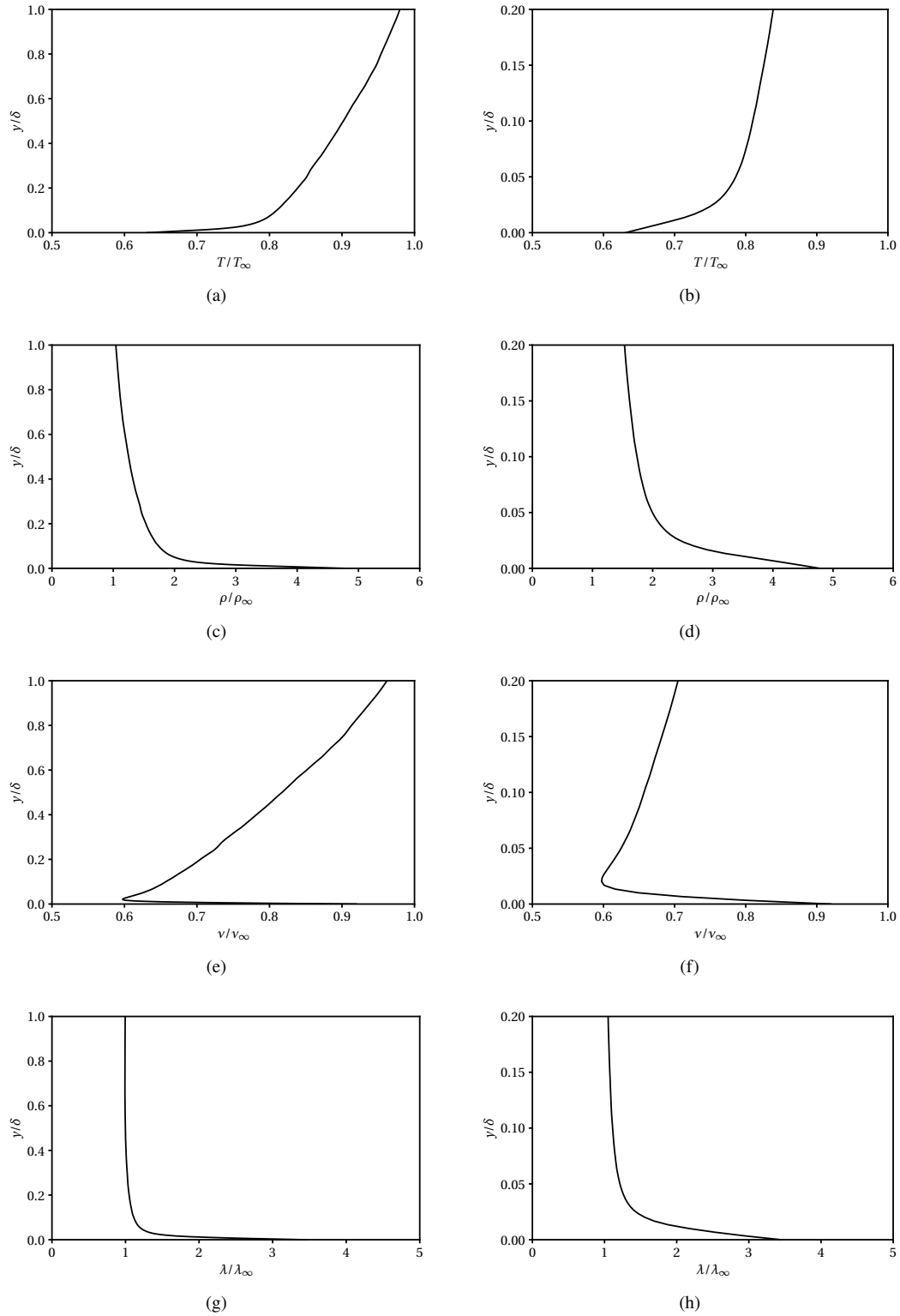

Fig. 12 Averaged flow properties within the turbulent boundary layer: (a) and (b) temperature, (c) and (d) density, (e) and (f) kinematic shear viscosity, and (g) and (h) thermal conductivity.

implies that the simulated boundary layer flow develops in the transcritical regime with pseudo phase change occurring when the *widom line* is crossed. The time advancement is conducted using the SSP-RK3 with the adaptive time step limited by CFL = 0.9. The shock capturing scheme is deactivated in the computational domain other than at the outlet buffer region, and no other types of artificial dissipation are imposed within the test region.

After reaching the statistically stationary stage, the flow quantities are analyzed over a time span of $\Delta t U_\infty/\delta_{\text{in}} \approx 16$ and in the z-direction. Mean velocity profile is shown in Fig. 11, where the y coordinate and u are scaled by the "law of the wall" quantities as $y^+ = y u_\tau/\nu_w$ and $u^+ = u/u_\tau$. ν_w is the kinematic viscosity at the wall, and u_τ is calculated as $u_\tau^2 = [\nu \partial u/\partial y]_w$. The observed behavior indicates that the simulation has achieved a realistic turbulent boundary layer state. Profiles of other flow properties within the boundary layer are shown in Fig. 12. The y-coordinate is scaled by the boundary layer thickness that corresponds to the 99% of the streamwise velocity, and the properties are scaled by those in the freestream. Due to the pseudo phase change, the density ratio is approximately 4.7 (Fig. 12d), and the density changes by more than a factor of two within 5% of the boundary layer thickness (associated with a temperature change that is less than 20% of freestream temperature). Additionally, the kinematic viscosity drops by more than 30% of the freestream viscosity within less than 2.5% of the boundary layer thickness, and a significant increase in thermal conductivity occurs as the fluid becomes subcritical. Further investigation of the turbulence behaviour in transcritical regime is the subject of on-going analysis. Additionally, grid-sensitivity study of the results are also being conducted.

V. Conclusions

A high-order compact finite difference based simulation framework has been applied to simulations of compressible dense gas flows near the critical condition. The solution system is fully conservative and closed by the Peng-Robinson p-v-T relation and the Chung et al. transport models. According to the staggered flux assembly using interpolated primitive variables, the computational results for nonlinear problems have significantly lower aliasing error than traditional collocated flux assembly. The divergence operation conducted by the edge-to-node staggered differencing scheme dramatically improves the accuracy of the viscous fluxes at small scales. Combined with the compact finite difference methods, high-order convergence, high spectral resolution, and robustness can be achieved without non-conservative correction or solution filtering. For highly compressible flow simulations, the central-Riemann hybrid fluxes can be used. The flux blending is controlled by physics-based shock sensor so that the numerical dissipation is highly localized at the shock structures without contaminating the simulation of the turbulent regions. The numerical performance of the simulation framework has been demonstrated in the simulation of a compressible supercritical shear layer flow at unity convective Mach number and a zero-pressure-gradient transcritical turbulent boundary layer flow with an isothermal wall. The results of the shear layer simulation are compared with those of the calorically perfect gas flow under the same flow conditions. Different solution behaviors are observed in the thermodynamic quantities associated with the shear layer growth. The boundary layer flow simulation results imply that a rapid change in the fluid properties occurs due to the pseudo phase change within a small portion of the turbulent boundary layer. Further grid refinement is needed for direct numerical simulations.

Acknowledgements

The authors are grateful to Professor Lluís Jofre Cruanyes for the helpful discussions on the implementation of the equation of state and transport models. This research is supported by the National Science Foundation (NSF), grant number NSF-OAC-2103509. The code development used resources from the Extreme Science and Engineering Discovery Environment (XSEDE), supported by NSF grant number NSF-ACI-1548562, and resources at the Texas Advanced Computing Center (TACC) at The University of Texas at Austin. The large-scale demonstrative simulations were supported by an ALCC allocation and run on the *Summit* supercomputer from the Oak Ridge Leadership Computing Facility at the Oak Ridge National Laboratory, which is supported by the Office of Science of the U.S. Department of Energy under Contract No. DE-AC05-00OR22725.

References

[1] Knez, Ž., Markočič, E., Leitgeb, M., Primožič, M., Hrnčič, M. K., and Škerget, M., "Industrial applications of supercritical fluids: A review," *Energy*, Vol. 77, 2014, pp. 235–243.

[2] Brunner, G., "Applications of supercritical fluids," *Annual Review of Chemical and Biomolecular Engineering*, Vol. 1, 2010, pp. 321–342.

[3] Ahn, Y., Bae, S. J., Kim, M., Cho, S. K., Baik, S., Lee, J. I., and Cha, J. E., "Review of supercritical CO2 power cycle technology and current status of research and development," *Nuclear engineering and technology*, Vol. 47, No. 6, 2015, pp. 647–661.

[4] Hickey, J.-P., Ma, P. C., Ihme, M., and Thakur, S. S., "Large eddy simulation of shear coaxial rocket injector: Real fluid effects," *49th AIAA/ASME/SAE/ASEE Joint PropulsionConference*, 2013, p. 4071.

[5] Kawai, S., Terashima, H., and Negishi, H., "A robust and accurate numerical method for transcritical turbulent flows at supercritical pressure with an arbitrary equation of state," *Journal of Computational Physics*, Vol. 300, 2015, pp. 116–135.

[6] Doehring, A., Kaller, T., Schmidt, S., and Adams, N., "Large-eddy simulation of turbulent channel flow at transcritical states," *International Journal of Heat and Fluid Flow*, Vol. 89, 2021, p. 108781.

[7] Schmitt, T., Selle, L., Ruiz, A., and Cuenot, B., "Large-eddy simulation of supercritical-pressure round jets," *AIAA journal*, Vol. 48, No. 9, 2010, pp. 2133–2144.

[8] Song, H., Ghate, A. S., Matsuno, K., West, J., Subramaniam, A., Brown, L. J., and Lele, S. K., "Robust high-resolution simulations of compressible turbulent flows without filtering," *AIAA Aviation 2022 Forum*, 2022, p. 4122.

[9] Peng, D.-Y., and Robinson, D. B., "A new two-constant equation of state," *Industrial & Engineering Chemistry Fundamentals*, Vol. 15, No. 1, 1976, pp. 59–64.

[10] WebBook, N., "Thermophysical properties of fluid systems," *Avaliable Online: http://webbook. nist. gov/chemistry/fluid/(access on 18 January 2015)*, 2016.

[11] Courant, R., Friedrichs, K., and Lewy, H., "Über die partiellen Differenzengleichungen der mathematischen Physik," *Mathematische annalen*, Vol. 100, No. 1, 1928, pp. 32–74.

[12] Chung, T. H., Ajlan, M., Lee, L. L., and Starling, K. E., "Generalized multiparameter correlation for nonpolar and polar fluid transport properties," *Industrial & engineering chemistry research*, Vol. 27, No. 4, 1988, pp. 671–679.

[13] Poling, B. E., Prausnitz, J. M., and O'connell, J. P., *Properties of gases and liquids*, McGraw-Hill Education, 2001.

[14] Lele, S. K., "Compact finite difference schemes with spectral-like resolution," *Journal of computational physics*, Vol. 103, No. 1, 1992, pp. 16–42.

[15] Nagarajan, S., Lele, S. K., and Ferziger, J. H., "A robust high-order compact method for large eddy simulation," *Journal of Computational Physics*, Vol. 191, No. 2, 2003, pp. 392–419.

[16] Shu, C.-W., and Osher, S., "Efficient implementation of essentially non-oscillatory shock-capturing schemes," *Journal of computational physics*, Vol. 77, No. 2, 1988, pp. 439–471.

[17] Rusanov, V. V., "The calculation of the interaction of non-stationary shock waves with barriers," *Zhurnal Vychislitel'noi Matematiki i Matematicheskoi Fiziki*, Vol. 1, No. 2, 1961, pp. 267–279.

[18] Jiang, G.-S., and Shu, C.-W., "Efficient implementation of weighted ENO schemes," *Journal of computational physics*, Vol. 126, No. 1, 1996, pp. 202–228.